Photoelectrochemical Detection of Glutathione by IrO2–Hemin–TiO2 Nanowire Arrays

7 AUTHORS, INCLUDING:

Biao Kong
Monash University (Australia)
41 PUBLICATIONS **759** CITATIONS

SEE PROFILE

Hao Wu
Fudan University
13 PUBLICATIONS **311** CITATIONS

SEE PROFILE

Photoelectrochemical Detection of Glutathione by IrO_2–Hemin–TiO_2 Nanowire Arrays

Jing Tang,[†] Biao Kong,[†] Yongcheng Wang, Ming Xu, Yanli Wang, Hao Wu, and Gengfeng Zheng*

Laboratory of Advanced Materials, Department of Chemistry, Fudan University, Shanghai, 200433, People's Republic of China

S Supporting Information

ABSTRACT: We have developed sensitive detection of glutathione using the IrO_2–hemin–TiO_2 nanowire arrays. Single-crystalline TiO_2 nanowires are synthesized by a hydrothermal reaction, followed by surface functionalization of ~3 nm thick hemin and ~1−2 nm diameter IrO_2 nanoparticles. The IrO_2–hemin–TiO_2 nanowire arrays offer much enhanced photocurrent with ~100% increase compared to the pristine TiO_2 nanowires and allow for label-free, real-time, sensitive photoelectrochemical detection of glutathione. The sensitivity achieved is ~10 nM in buffer, comparable to or better than most of the existing glutathione detection methods. Furthermore, cell extracts containing glutathione are robustly detected, with ~8000 cells/mL for HeLa cells and ~5000 cells/mL for human embryonic kidney 293T cells. This nanowire PEC sensor assay exhibits excellent selectivity and stability, suggesting a potential detection platform for analyzing the glutathione level in biosamples.

KEYWORDS: Glutathione, nanowire, IrO_2–hemin–TiO_2, photoelectrochemical, biosensing
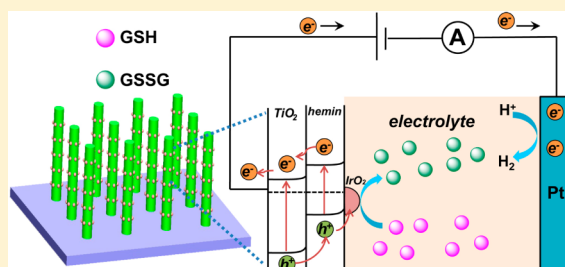
Glutathione (GSH) is an important thiolated tripeptide and endogenous antioxidant and exists widely in the intracellular environment.[1−3] The level of GSH is associated with many diseases including aging and cancer.[4] A number of methods have been developed to interrogate the GSH level inside cells, including luminescence analysis,[2] fluorometry,[5] colorimetry,[6] and electrochemistry.[7] The photoelectrochemical (PEC) method, a recently developed detection approach, uses light and electricity energy for the sensor excitation and detection, respectively, thus enabling efficient reduction of some undesired background noise and increasing sensitivity.[8] The photon-to-charge conversion process of the photoactive materials, such as organic dyes[5] and inorganic semiconductor materials,[9] is highly sensitive to the surface chemistry and microenvironment fluctuation.[10] In particular, TiO_2 is a substantially attractive candidate for the PEC detection, due to its strong optical absorption, high chemical stability, environmental benignity, and low cost.[11] Nonetheless, the capability of the TiO_2-based PEC detection is still limited by its predominant absorption in the UV region,[12] low electron mobility (0.3 cm^2 V^{-1} s^{-1} for rutile TiO_2),[13] and sluggish kinetics of holes.[14] Several research discoveries have recently been developed to improve the performance of the TiO_2-based PEC method. For example, hemin, a synthetic molecule that mimics the natural enzyme,[15,16] is also an excellent light absorber that can increase the absorption of TiO_2 in the visible range.[17] The functionalization of TiO_2 nanoparticle (NP) surface with hemin has been demonstrated for analyzing the GSH level with rapid response and good reproducibility.[18] However, the charge carrier transfer across numerous grain boundaries between individual NPs results in substantially high

charge recombination rates and reduced PEC sensitivity. On the other hand, one-dimensional (1D) nanostructures such as nanowires (NWs) and nanotubes (NTs) can provide fast charge transport through the micrometer-scale axial lengths, while at the same time enabling efficient charge separation across the nanometer-scale diameters.[19] The PEC detection assays based on TiO_2 NWs/NTs have been demonstrated for H_2O_2,[8] rabbit immunoglobulin G (IgG),[20] prostate specific antigen (PSA),[21] adenosine,[22] and others. Moreover, the incorporation of IrO_2 with TiO_2 can facilitate the hole transfer process, leading to an enhanced PEC conversion efficiency.[23,24] However, to the best of our knowledge, a multicomponent PEC platform that simultaneously addresses the improved light absorption, enhanced charge transport, and IrO_2 catalytic property, for the capability of sensitive detection of functional biomolecules, has not been demonstrated yet.

In this Letter, we demonstrate the synthesis and surface functionalization of hemin and IrO_2 NPs on hydrothermally grown TiO_2 NWs and use these NWs for the label-free, sensitive detection of GSH as a biomolecule model. PEC measurements show that the IrO_2/hemin-coated TiO_2 NWs exhibit a photocurrent of ~1.4 mA/cm^2 at 1 sun illumination, which is a ~100% increase from that of the pristine TiO_2 NWs, attributed to the enhanced photoabsorption and increased charge carrier density. The real-time sensing experiments show that the obtained IrO_2–hemin–TiO_2 NWs can detect free GSH at a minimum concentration of 10 nM, with high
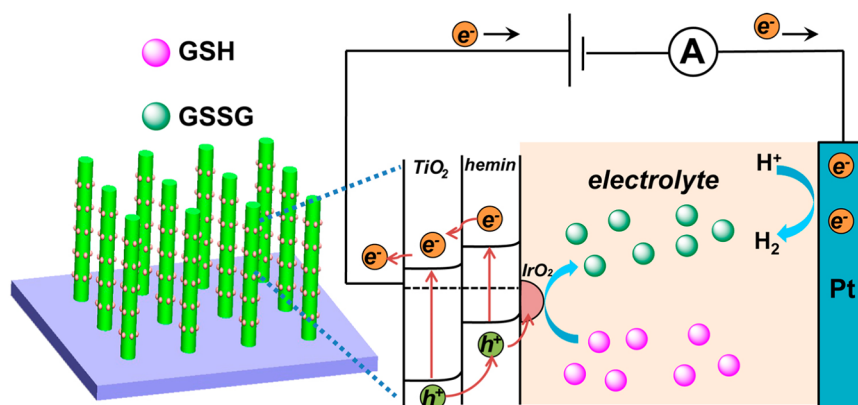
Figure 1. Schematic illustration of the PEC process for GSH detection by an IrO_2−hemin−TiO_2 NW biosensor.

selectivity and stability, and can be carried out in examining the GSH concentrations in cellular extracts or serum.

The PEC biosensing process of the IrO_2−hemin−TiO_2 NWs for the GSH detection is schematically shown in Figure 1. The electron transfer from the excited state of hemin to the conduction band of TiO_2 is thermodynamically favorable, as the oxidation potential of the excited state of hemin is higher than the conduction band energy level of TiO_2.[18] In addition, hemin can specifically recognize the presence of GSH,[18] which acts as the electron donor to the holes located on the excited state of hemin. These electrons can then quickly be injected into the conduction band of the TiO_2 NWs,[18] which are subsequently transferred to the fluorine-doped tin oxide (FTO) electrode, leading to an increase of the photocurrent. During this process, GSH is oxidized to glutathione disulfide (GSSG).

The hydrothermal growth of pristine TiO_2 NWs on FTO glass substrates has been described elsewhere[25] and used in our experiment (Methods in the Supporting Information). After the growth, the whole FTO substrate is uniformly covered by a white thin film. Scanning electron microscopy (SEM) images show that these as-synthesized TiO_2 NW arrays are highly uniform, normal to the growth substrate, and packed over the entire field of view (Figures S1 and S2). The average diameter and length of these NWs are around 100−150 nm and 1.5−2 μm, respectively, and are well-tuned by different synthesis conditions.[11] The side-view images of the NW array sample (Figure S2b) confirm that all NWs are grown almost perpendicularly from the FTO substrate. Figure S3 represents the synthesis and surface modification of the IrO_2−hemin−TiO_2 NW approach. The TiO_2 surface is linked with a layer of amine-terminated silane (3-aminopropyl triethoxysilane, APTES),[26] which subsequently conjugates with hemin via a linker chemistry using N-hydroxysuccinimide (NHS) and 1-(3-dimethylaminopropyl)-3-ethylcarbodiimide hydrochloride (EDC·HCl) (Methods in the Supporting Information). Transmission electron microscopy (TEM) images show that the surface of each TiO_2 NW is covered with a thin amorphous layer of ∼3 nm (Figure S2c). After that, IrO_2 NPs are deposited onto the hemin−TiO_2 NW surface via a facile chemical bath deposition method (Methods in the Supporting Information).[23] The NW surface is covered by a layer of ∼1−2 nm NPs, revealed by high-resolution TEM (HRTEM) images (Figure 2c, S4). The TiO_2 NWs show a clear single crystalline structure (Figure S2d), with a well-resolved lattice spacing of 0.324 and 0.248 nm, in accord with the d-spacing values of rutile TiO_2 in (110) and (101) planes, respectively. The energy
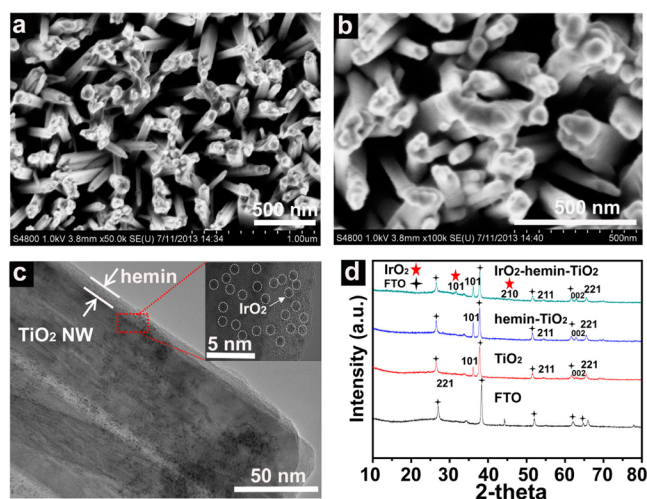

Figure 2. (a, b) SEM images of the IrO_2−hemin−TiO_2 NW arrays on a FTO glass substrate. (c) TEM image of an IrO_2−hemin−TiO_2 NW. Inset: IrO_2 NPs with ∼1−2 nm-diameter on the NW surface, highlighted by the white circles. (d) XRD patterns of FTO (black curve), TiO_2 NWs (red curve), hemin−TiO_2 NWs (blue curve), and IrO_2−hemin−TiO_2 NWs (green curve).

dispersive X-ray spectroscopy (EDX) shows that the atomic percentage of Fe and Ir in a representative IrO_2−hemin−TiO_2 NW are ∼0.11% and ∼0.45%, respectively (Figure S5).

X-ray diffraction (XRD) spectroscopy further confirms that the IrO_2−hemin−TiO_2 NWs have a rutile TiO_2 crystal structure, same as the pristine TiO_2 NWs (Figure 2d). All of the diffraction peaks from the hemin−TiO_2 and TiO_2 NW samples are in good accord with the tetragonal rutile phase (JCPDS No. 21-1276). Additional peaks of IrO_2 are observed from the IrO_2−hemin−TiO_2 NWs (JCPDS No. 15-0870). Fourier transformation infrared (FTIR) spectroscopy is further used to characterize the IrO_2−hemin−TiO_2 NWs (Figure S6). In comparison with the FTIR spectra of TiO_2 NWs and hemin, the FTIR spectrum of the IrO_2−hemin−TiO_2 NWs displays obvious absorption peaks corresponding to the amide band I (1697 cm^{-1}) of hemin, which indicates that hemin is successfully linked on the TiO_2 NWs by the amidation reaction.

The photocurrent measurements of the IrO_2−hemin−TiO_2 NWs are first carried out to evaluate the potential as PEC biosensors (Methods in the Supporting Information). In a potential window between −1 and 0.4 V vs Ag/AgCl, the photocurrent densities of the pristine TiO_2 NW and the IrO_2−
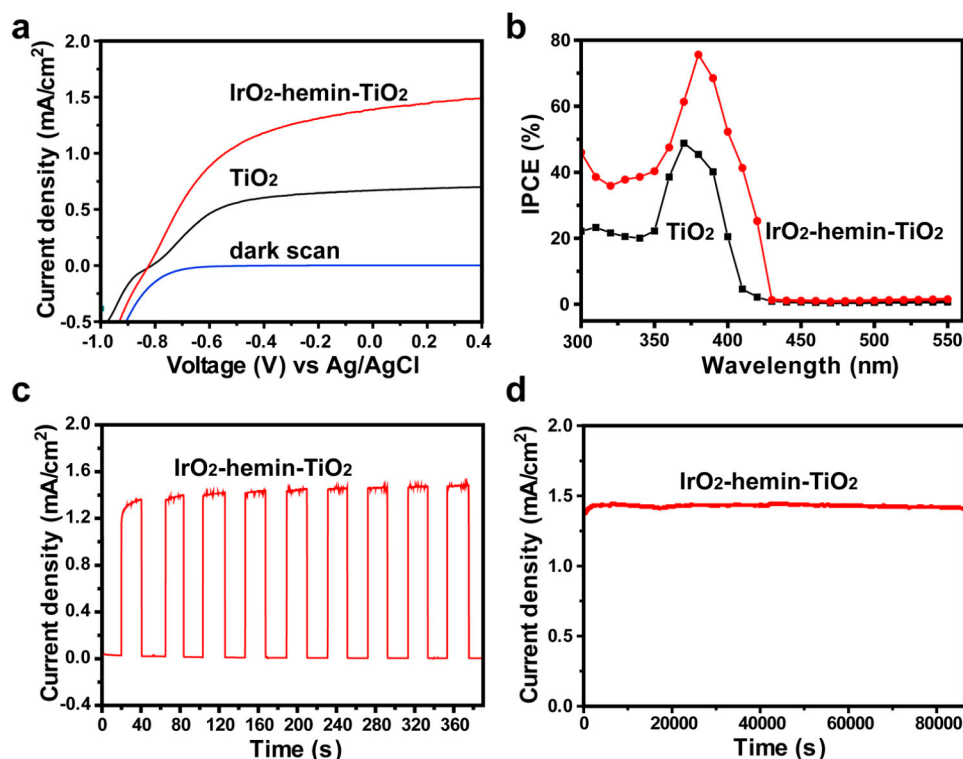
Figure 3. (a) Line sweep voltammograms measured from the pristine TiO_2 NWs (black curve) and the IrO_2−hemin−TiO_2 NWs (red curve). The dark current of the IrO_2−hemin−TiO_2 NWs (blue curve) is also plotted for comparison. (b) IPCE curves of the pristine TiO_2 NWs (black curve) and the IrO_2−hemin−TiO_2 NWs (red curve). (c) Time-dependent photocurrent density of the IrO_2−hemin−TiO_2 NW photoanode at repeated on/off cycles of simulated sunlight illumination. (d) Time-dependent photocurrent density of the same IrO_2−hemin−TiO_2 NW photoanode under a continuous simulated sunlight illumination.

hemin−TiO_2 NW array are 0.69 and 1.40 mA/cm^2 at 0 V vs Ag/AgCl, respectively (Figure 3a). The incident-photon-to-current conversion efficiency (IPCE) measurement shows that the pristine TiO_2 NWs have an IPCE value of 20−40% around 200−400 nm, which quickly drops to zero for wavelength above 400 nm (Figure 3b). In contrast, the IPCE value of the IrO_2−hemin−TiO_2 NWs shows a significant increase to 40−80% around 200−400 nm, with a peak value of 80% at ~380 nm, and then drops to zero for wavelength above 430 nm. This increased photoactivity in both the visible and UV regions can partly be attributed to the enhanced light absorption by hemin, as the UV−vis spectrum of hemin shows a similar absorption profile (Figure S7), which is consistent with literature.[27] Finally, the time-dependent photocurrent measurement of the IrO_2−hemin−TiO_2 NWs shows that the photocurrent density is highly stable for >24 h and well-correlated with the simulated solar light (Figure 3c,d), indicating the structural stability of the IrO_2−hemin−TiO_2 NWs and their potential for biosensing experiments.

For the biosensing of GSH, a bias of 0.2 V is applied to minimize the interference of other reductive species coexisting in the samples.[18] Although the electrochemical oxidation of GSH at the IrO_2−hemin−TiO_2 NW starts at 0.2 V, the slow electron-transfer rate in the oxidation process of GSH leads to a high overpotential, and thus no obvious oxidation peak is observed until the potential is scanned to 1.0 V, as shown in the cyclic voltammogram (CV) of the IrO_2−hemin−TiO_2 NWs (Figure S8). The response of the IrO_2−hemin−TiO_2 to GSH is then interrogated by the time-dependent current measurement under a bias of 0.2 V. Figure 4a shows a typical amperogram obtained by successive additions of GSH at intervals, with a

final GSH concentration increase of ~10 nM in the PEC cell each time. Upon each addition of GSH, the IrO_2−hemin−TiO_2 NW electrode responds quickly with a similar conductance increase, which reaches equilibrium within 5−10 s. For comparison, pristine TiO_2 NWs without the surface functionalization of hemin do not show signals to the addition of GSH (Figure S9). The conductance change with different GSH concentrations and the corresponding calibration curves are summarized in Figure 4b. A linear range of 10 nM to 10 μM is obtained, with the lowest GSH concentration detected as 10 nM. This sensitivity is comparable or better than most of the GSH detection methods reported previously (Table S1).

The selectivity of the IrO_2−hemin−TiO_2 NW-based PEC sensor is confirmed by measuring the responses for other amino acids, metal ions, as well as common chemical/biological interferences, showing much smaller or negligible signals compared to that of GSH (Figure 4c−e). For instance, the addition of ascorbic acid (AA), dopamine (DA), or uric acid (UA) at a concentration of 100 μM does not give rise to observable signal, while a significant current response is obtained for the subsequent addition of GSH (Figure S10). Furthermore, the repeating test of the IrO_2−hemin−TiO_2 NW-based PEC biosensors for over 30 days shows that over 90% of the initial photocurrent response is maintained (Figure 4f), suggesting excellent stability and reproducibility of the NW biosensor. The superior sensing performance and long-term function stability of the IrO_2−hemin−TiO_2 NW biosensor are attributed to the stable structure and excellent biocompatibility of TiO_2 and IrO_2, as well as the strong chemical interaction between hemin and TiO_2.
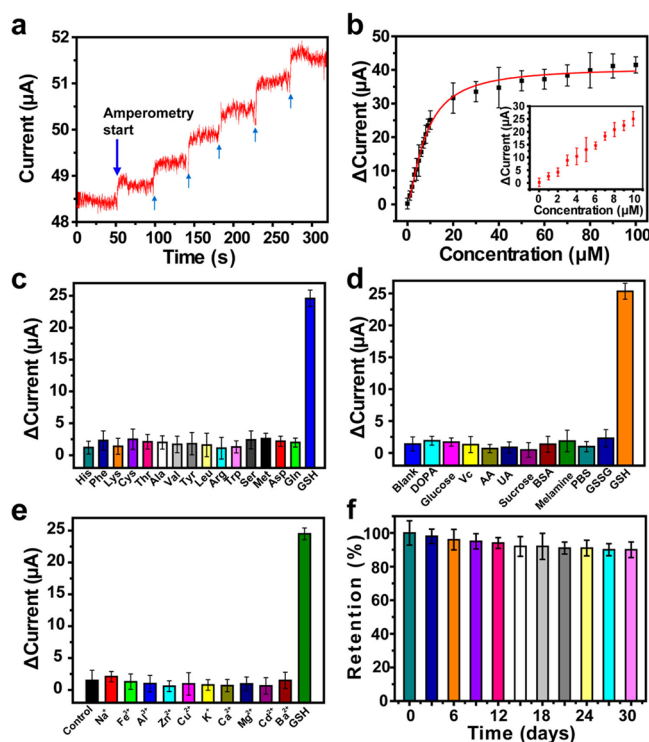
Figure 4. (a) Current versus time data of an IrO_2–hemin–TiO_2 NW biosensor for successive addition of GSH (with a final concentration increase of 10 nM each time, indicated by the blue arrows) to buffer (pH 7.4) at 0.2 V under 100 mW/cm^2 simulated sunlight illumination. The size of the active sample area was 0.032 cm^2. (b) Calibration sensing signal versus the GSH concentration, fitted with the Langmuir curve (red curve). Inset: Zoom-in for the low concentration range between 10 nM and 10 μM. (c–e) Photocurrent response of the IrO_2–hemin–TiO_2 biosensor in the presence of (c) amino acids, (d) common chemical/biological interferences, and (e) different metal ions, each with concentrations of ~100 μM. (f) The stability test of an IrO_2–hemin–TiO_2 NW biosensor over one month.

The IrO_2–hemin–TiO_2 NW biosensor is further studied for the PEC detection of the GSH extracts from living cells, including human embryonic kidney (HEK) 293T cells (a normal cell line) and HeLa cells (Methods in the Supporting Information). To verify the performance of the PEC sensor in the determination of HeLa cell quantity, the photocurrent response with different HeLa cell numbers (from 8000 to 5 × 10^5 cells/mL) is measured and summarized (Figure 5a, b), with a detection limit of 8000 cells/mL. Under otherwise same conditions, for the HEK 293T cells, the IrO_2–hemin–TiO_2 NW biosensor shows an observable amperometric response after the addition of cell extracts, with a lower detection limit of 5000 cells/mL (Figure S11). The higher signal from HEK 293T cells suggests a more active cellular activity than that of HeLa cells. These results are in good accord with previous reports, as normal cells conserve high levels of GSH and protein thiols, while cancer cells caused by oxidative stress can induce depletion of GSH and a severe decline in concentration of protein thiols.[28]

Finally, the delivery of GSH in a mouse serum to the IrO_2–hemin–TiO_2 NW biosensor assay (with 1:200 dilution in phosphate buffer) leads to a PEC signal, with the lowest detectable concentration of ~200 nM (Figure 5c), suggesting the potential of direct GSH detection in complex body fluids. Moreover, the introduction of N-ethylmaleimide (NEM) into
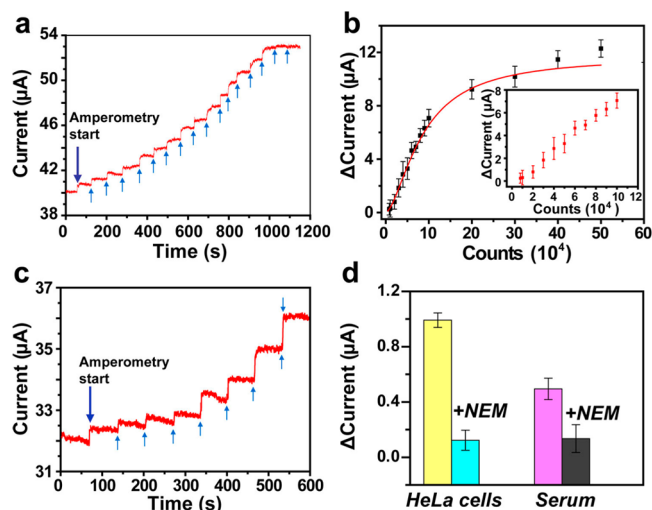

Figure 5. (a) Current versus time data of an IrO_2–hemin–TiO_2 NW biosensors for extracts from solutions of HeLa cells (with a final concentration increase of 10 000 cells/mL each time, indicated by the blue arrows). The size of the active sample area was 0.028 cm^2. (b) The calibration sensing signal versus the HeLa cell number, fitted with the Langmuir curve (red curve). Inset: Zoom-in for the low concentration range. (c) Current versus time data of the IrO_2–hemin–TiO_2 NW biosensors for GSH detection in serum (with 1:200 dilution in buffer). The size of the active sample area was 0.025 cm^2. (d) Cellular assay and GSH detection in serum and HeLa cell extracts. Columns presented (from left to right): pristine HeLa cell extracts (yellow bar), mixture of HeLa cell extracts and NEM (blue bar), serum containing GSH (red bar), and serum containing both GSH and NEM (black bar).

both the cell extracts and GSH-containing serum reduces the current change to the background level (Figure 5d). As NEM is a well-known thiol-blocking agent and selectively decomposes GSH,[29] this result indicates that the current increase of the IrO_2–hemin–TiO_2 NW biosensor is attributed to the GSH produced inside cells, which strongly suggests the potential application of the IrO_2–hemin–TiO_2 NWs as a sensitive PEC biosensor for GSH.

In summary, we have developed a highly robust PEC biosensing platform of the IrO_2–hemin–TiO_2 NWs, which are fabricated by a facile hydrothermal synthesis of TiO_2 NWs, followed by the surface functionalization of hemin and the chemical bath deposition of IrO_2 NPs. Hemin can efficiently increase the light absorption and selectively recognize the GSH targets, and the IrO_2 NPs can effectively increase the charge transfer kinetics, leading to a ~ 100% increase of photocurrent compared to the pristine TiO_2 NWs. Using GSH as a model, the IrO_2–hemin–TiO_2 NWs exhibit excellent PEC sensing performance for the detection of free GSH in buffers, GSH from cell extracts and in serum, with a low applied potential, wide detection range, high selectivity, and high reproducibility. Further studies and developments of these hemin-functionalized TiO_2 NWs may allow for more opportunities for the construction of a variety of novel PEC biosensors with fast response, enhanced specificity, and long-term stability.

■ ASSOCIATED CONTENT

S Supporting Information

Details of methods and supporting figures. This material is available free of charge via the Internet at http://pubs.acs.org.

■ AUTHOR INFORMATION

Corresponding Author
*E-mail: gfzheng@fudan.edu.cn.

Author Contributions
†J.T. and B.K. contributed equally to this work.

Notes
The authors declare no competing financial interest.

■ REFERENCES

(1) Gutscher, M.; Pauleau, A.-L.; Marty, L.; Brach, T.; Wabnitz, G. H.; Samstag, Y.; Meyer, A. J.; Dick, T. P. *Nat. Methods* **2008**, *5*, 553–559.

(2) Deng, R.; Xie, X.; Vendrell, M.; Chang, Y.-T.; Liu, X. *J. Am. Chem. Soc.* **2011**, *133*, 20168–20171.

(3) Huang, R.; Wang, X.; Wang, D.; Liu, F.; Mei, B.; Tang, A.; Jiang, J.; Liang, G. *Anal. Chem.* **2013**, *85*, 6203–6207.

(4) Fruehauf, J. P.; Meyskens, F. L. *Clin. Cancer Res.* **2007**, *13*, 789–794.

(5) Niu, L. Y.; Guan, Y. S.; Chen, Y. Z.; Wu, L. Z.; Tung, C. H.; Yang, Q. Z. *J. Am. Chem. Soc.* **2012**, *134*, 18928–18931.

(6) Durocher, S.; Rezaee, A.; Hamm, C.; Rangan, C.; Mittler, S.; Mutus, B. *J. Am. Chem. Soc.* **2009**, *131*, 2475–2477.

(7) Wang, Y.; Lu, J.; Tang, L.; Chang, H.; Li, J. *Anal. Chem.* **2009**, *81*, 9710–9715.

(8) Chen, D.; Zhang, H.; Li, X.; Li, J. *Anal. Chem.* **2010**, *82*, 2253–2261.

(9) Wang, G.; Yang, X.; Qian, F.; Zhang, J. Z.; Li, Y. *Nano Lett.* **2010**, *10*, 1088–1092.

(10) Chen, X.; Mao, S. S. *Chem. Rev.* **2007**, *107*, 2891–2959.

(11) Xu, M.; Da, P.; Wu, H.; Zhao, D.; Zheng, G. *Nano Lett.* **2012**, *12*, 1503–1508.

(12) Wang, G.; Wang, H.; Ling, Y.; Tang, Y.; Yang, X.; Fitzmorris, R. C.; Wang, C.; Zhang, J. Z.; Li, Y. *Nano Lett.* **2011**, *11*, 3026–3033.

(13) Hwang, Y. J.; Hahn, C.; Liu, B.; Yang, P. *ACS Nano* **2012**, *6*, 5060–5069.

(14) Tang, J.; Durrant, J. R.; Klug, D. R. *J. Am. Chem. Soc.* **2008**, *130*, 13885–13891.

(15) Xue, T.; Jiang, S.; Qu, Y.; Su, Q.; Cheng, R.; Dubin, S.; Chiu, C. Y.; Kaner, R.; Huang, Y.; Duan, X. *Angew. Chem., Int. Ed.* **2012**, *51*, 3822–3825.

(16) Jiang, S.; Cheng, R.; Wang, X.; Xue, T.; Liu, Y.; Nel, A.; Huang, Y.; Duan, X. *Nat. Commun.* **2013**, *4*, 2225.

(17) Yella, A.; Lee, H.-W.; Tsao, H. N.; Yi, C.; Chandiran, A. K.; Nazeeruddin, M. K.; Diau, E. W.-G.; Yeh, C.-Y.; Zakeeruddin, S. M.; Grätzel, M. *Science* **2011**, *334*, 629–634.

(18) Tu, W.; Dong, Y.; Lei, J.; Ju, H. *Anal. Chem.* **2010**, *82*, 8711–8716.

(19) Greenham, N. C.; Peng, X.; Alivisatos, A. P. *Phys. Rev. B* **1996**, *54*, 17628.

(20) Mun, K. S.; Alvarez, S. D.; Choi, W.-Y.; Sailor, M. J. *ACS Nano* **2010**, *4*, 2070–2076.

(21) Zhao, W. W.; Ma, Z. Y.; Yan, D. Y.; Xu, J. J.; Chen, H. Y. *Anal. Chem.* **2012**, *84*, 10518–10521.

(22) Tian, C. Y.; Xu, J. J.; Chen, H. Y. *Chem. Commun.* **2012**, *48*, 8234–8236.

(23) Liu, C.; Tang, J.; Chen, H. M.; Liu, B.; Yang, P. *Nano Lett.* **2013**, *13*, 2989–2992.

(24) Moore, G. F.; Blakemore, J. D.; Milot, R. L.; Hull, J. F.; Song, H.-E.; Cai, L.; Schmuttenmaer, C. A.; Crabtree, R. H.; Brudvig, G. W. *Energy Environ. Sci.* **2011**, *4*, 2389–2392.

(25) Liu, B.; Aydil, E. S. *J. Am. Chem. Soc.* **2009**, *131*, 3985–3990.

(26) Dixit, C. K.; Vashist, S. K.; MacCraith, B. D.; O'Kennedy, R. *Nat. Protocols* **2011**, *6*, 439–445.

(27) Guo, Y.; Deng, L.; Li, J.; Guo, S.; Wang, E.; Dong, S. *ACS Nano* **2011**, *5*, 1282–1290.

(28) Tang, B.; Xing, Y.; Li, P.; Zhang, N.; Yu, F.; Yang, G. *J. Am. Chem. Soc.* **2007**, *129*, 11666–11667.

(29) Lim, C. S.; Masanta, G.; Kim, H. J.; Han, J. H.; Kim, H. M.; Cho, B. R. *J. Am. Chem. Soc.* **2011**, *133*, 11132–11135.